



Cite this: *Nanoscale*, 2023, **15**, 3243

Received 21st October 2022,  
Accepted 19th January 2023

DOI: 10.1039/d2nr05838c  
[rsc.li/nanoscale](http://rsc.li/nanoscale)

## A sprayed graphene transistor platform for rapid and low-cost chemical sensing†

Benji Fenech-Salerno, <sup>a</sup> Martin Holicky, <sup>a</sup> Chengning Yao, <sup>a</sup> Anthony E. G. Cass <sup>a</sup> and Felice Torrisi <sup>a,b</sup>

We demonstrate a novel and versatile sensing platform, based on electrolyte-gated graphene field-effect transistors, for easy, low-cost and scalable production of chemical sensor test strips. The Lab-on-PCB platform is enabled by low-boiling, low-surface-tension sprayable graphene ink deposited on a substrate manufactured using a commercial printed circuit board process. We demonstrate the versatility of the platform by sensing pH and  $\text{Na}^+$  concentrations in an aqueous solution, achieving a sensitivity of  $143 \pm 4 \mu\text{A}$  per pH and  $131 \pm 5 \mu\text{A}$  per  $\log_{10}\text{Na}^+$ , respectively, in line with state-of-the-art graphene chemical sensing performance.

### 1. Introduction

The rapid ever-growing need for improved chemical and biological sensing platforms has ushered in a race for diagnostic technologies.<sup>1,2</sup> The applications span beyond health, and include environmental monitoring, agriculture, and food processing industry,<sup>3–6</sup> requiring sensors to satisfy a range of criteria, such as being sensitive and selective to analytes within diagnostically-relevant ranges, in real-time, at a low-cost, and easy to operate by the end user.<sup>7</sup>

Chemical sensors (also known as chemosensors) are a broad family of sensors which are used to extract information on the chemical composition of a sample.<sup>8</sup> In particular, electrochemical sensors are among the largest and oldest class of chemical sensors, whereby the measurand is detected as a measurable current (amperometry or voltammetry), measurable potential (potentiometry) or measurable change in the conductive properties of a medium between electrodes (conductometry).<sup>9</sup> All three sensor architectures have reached commercial maturity, with devices such as the amperometric glucose sensor,<sup>10</sup> potentiometric ion sensors<sup>11</sup> and conductometric vapour sensors.<sup>12</sup>

New materials enable a wide range of sensors to be created.<sup>13–17</sup> Graphene, a single layer of carbon atoms arranged

in a hexagonal lattice, has been successfully used in a wide variety of sensors ranging from simple ion detection, through gas sensing to highly specific and sensitive biomolecule recognition.<sup>18–20</sup> Graphene has various highly attractive properties for sensing, including an extremely high surface to volume ratio yielding excellent sensitivity<sup>21</sup> and easy functionalisation due to its carbon chemistry.<sup>22</sup>

A range of electrochemical sensors can be constructed using graphene – for instance potentiometric, where the voltage between graphene film and a reference electrode is measured and can be used for the determination of ions and organic molecules.<sup>23,24</sup> Graphene chemiresistive sensors use the change in electrical resistance of graphene film to perform gas sensing.<sup>25</sup> Graphene can also be used as the channel in a field-effect transistor (FETs) which allows for very sensitive and fast detection over tunable, diagnostically relevant ranges.<sup>26,27</sup>

A graphene FET (GFET) consists of a graphene film across the source and drain electrodes forming the FET channel with the gate electrode separated by either a dielectric (dielectric-gated GFET, DG-GFET) or an electrolyte (electrolyte-gated GFET, EG-GFET, also referred to as solution-gated GFET, SG-GFET or liquid-gated GFET, LG-GFET).<sup>27</sup> In both cases, a potential applied at the gate electrode can modulate the current flowing through the graphene channel due to the field effect.<sup>27</sup> In the case of EG-GFETs, the actual gate voltage seen by the channel is affected by the double layer capacitance, graphene quantum capacitance and electrochemical potentials which enable the sensing of various analytes.<sup>28–31</sup>

The selectivity of GFET sensors is enabled by the functionalisation of the channel or the gate with a receptor molecule responding to a particular analyte. The breadth of receptor structures used is extensive and includes enzymes,<sup>32</sup> apta-

<sup>a</sup>Imperial College London, Department of Chemistry, Molecular Sciences Research Hub, 82 Wood Lane, London W12 0BZ, UK. E-mail: [f.torrisi@imperial.ac.uk](mailto:f.torrisi@imperial.ac.uk)

<sup>b</sup>Dipartimento di Fisica e Astronomia, Università di Catania & CNR-IMM (Catania Università), Via S. Sofia 64, 95123 Catania, Italy

† Electronic supplementary information (ESI) available. See DOI: <https://doi.org/10.1039/d2nr05838c>

‡ These authors contributed equally.



mers,<sup>33</sup> antibodies,<sup>34</sup> peptide nucleic acids,<sup>35</sup> single-strand deoxyribonucleic acid (ssDNA)<sup>36</sup> and ion-selective membranes (ISMs).<sup>37</sup>

The graphene channel in EG-GFET sensors is typically achieved by chemical vapour deposition (CVD) of graphene on a copper foil and subsequent transfer of the graphene onto the desired substrate.<sup>38,39</sup> However, a simpler and scalable approach is available through solution-processable graphene inks which are prepared by liquid-phase exfoliation (LPE) through sonication,<sup>40–42</sup> shear mixing<sup>43</sup> or microfluidisation<sup>44</sup> of graphite. The resulting inks can be then deposited by spray-coating,<sup>45</sup> ink-jet printing,<sup>46</sup> screen-printing<sup>47</sup> or aerosol-jet printing.<sup>48</sup> This forms thin films consisting of a network of single-layer graphene (SLG) and few-layer graphene (FLG) flakes with average flake thickness varying from 2 to 10 nm (ref. 44, 49 and 50) and carrier mobility of up to  $150 \text{ cm}^2 \text{ V}^{-1} \text{ s}^{-1}$ .<sup>49</sup> However, unlike CVD graphene, LPE graphene has only seen limited use in EG-GFET sensors<sup>51</sup> despite its obvious advantages in terms of ink production scalability and the ease of its deposition.<sup>52</sup>

Rapid prototyping and scalable manufacturing of commercial chemical sensing test strips requires the sensors to be accurate and precise.<sup>53</sup> These factors are strongly influenced by the device substrate and electrode design.<sup>54</sup> For EG-FETs, the electrodes need to be electrochemically inert, typically made from gold.<sup>27</sup> The geometry of the channel and the ratio of its width ( $W$ ) to length ( $L$ ) impact the overall channel resistance and the signal to noise ratio.<sup>54</sup> Shorter channel length or longer channel width at a constant channel area result in higher currents at a given drain-source voltage ( $V_{DS}$ )<sup>54</sup> which then enables clear separation between the currents flowing through the graphene that are relevant to sensing and any leakage currents flowing through the electrolyte. A commercial printed circuit board (PCB) manufacturing process can provide repeatable and well-defined electrodes with sufficiently high resolution ( $<100 \mu\text{m}$ ) enabling the manufacture of short and wide-channel electrodes, at an industrial scale.<sup>55</sup>

In this work, we present a novel route to manufacture EG-GFET test strips using PCB technology. We develop, a commercial and accessible process to obtain scalable and low-cost EG-GFETs deposited by spray-coating. The function of such devices is demonstrated by detecting two analytes, pH and  $\text{Na}^+$ , which are relevant for a wide range of fields, for instance, point-of-care diagnostics,<sup>56</sup> agriculture<sup>57</sup> and environmental monitoring.<sup>58</sup> The sensor devices are characterised in terms of their sensitivity, selectivity, limit-of-detection (LOD), limit of quantification (LOQ), resolution, response time ( $\tau_r$ ) and linear range (see 'Methods').

## 2. Results and discussion

### Synthesis & characterisation of the graphene ink

We select spray-coating as the deposition technique for our graphene ink, as this is a non-contact technique compatible with high-throughput manufacturing.<sup>59</sup> Spray-coating requires

inks with a boiling point between 50 and 100 °C and a surface tension as low as possible.<sup>45,60</sup> For the graphene ink we select 2-propanol (IPA), which has a boiling point of 82 °C (ref. 61) and a surface tension of only  $20.34 \text{ mN m}^{-1}$ , satisfying both criteria. From the wide range of possible graphene ink preparation methods,<sup>50,62–64</sup> we select sonication-assisted LPE due to its simplicity and compatibility with low-boiling solvents.<sup>52</sup> We sonicate 500 mg of graphite in 50 mL IPA for 9 hours stabilised by small quantities (20 mg) of the biocompatible polyvinylpyrrolidone (PVP) to enable achieving the required concentration and improving the ink shelf life.<sup>65</sup> The dispersion is then centrifuged at 13 000g to remove residual unexfoliated flakes, as further detailed in 'Methods'.

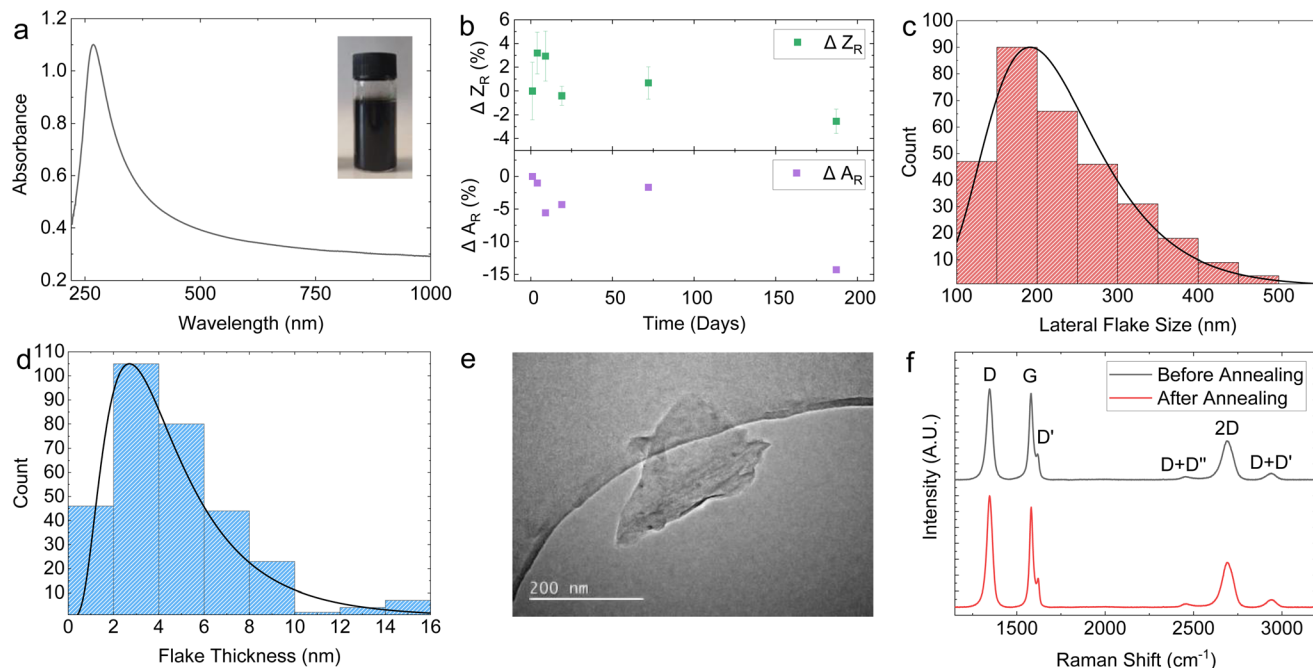
Whilst the PVP stabiliser increases the concentration and stability of the ink, it is known to lower the conductivity of the nanostructured graphene thin films as it is electrically insulating.<sup>66</sup> PVP decomposes into gaseous products when heated to temperatures above 375 °C (Fig. S1†) but such high temperatures are above the decomposition temperature of the PCB substrate.<sup>67</sup> PVP removal can be also achieved by a xenon intense pulsed light (IPL) source degrading the polymer<sup>68</sup> which is the method of choice for this work.

Fig. 1a shows the optical absorption spectrum (OAS) of the graphene ink, with an inset of the undiluted ink in the top right corner. The shape of the OAS in Fig. 1a is typical for graphene inks with flat absorption in the visible portion of the spectrum and a peak in the UV region corresponding to the van Hove singularity at the M point of the Brillouin zone in graphene.<sup>69</sup> Applying the Beer-Lambert law  $A = \epsilon cl$  where  $A$  is the absorbance,  $l$  is the path length and  $\epsilon$  is the absorption coefficient ( $2460 \text{ L g}^{-1} \text{ m}^{-1}$  at 660 nm),<sup>40</sup> we can estimate flake concentration  $c$  as  $0.818 \text{ mg mL}^{-1}$  for our graphene ink. Given the high centrifugation acceleration of 13 000g, this concentration is an order of magnitude higher than other PVP graphene inks reported in the literature, as outlined in ESI Table S1.†

The rheology of the graphene ink is investigated to assess its suitability for spray coating. The surface tension ( $\gamma$ ) of the prepared graphene ink was  $\gamma \sim 18.50 \pm 0.25 \text{ mN m}^{-1}$  (Fig. S2†), lower than  $\sim 20.34 \text{ mN m}^{-1}$  for pure 2-propanol at 25 °C, due to the added PVP stabiliser. Conversely, the resulting dynamic viscosity  $\eta \sim 2.35 \pm 0.1 \text{ mPa s}$  is higher than  $\sim 2.01 \text{ mPa s}$  for the pure 2-propanol<sup>70</sup> due to the presence of the stabiliser and the concentration of the graphene flakes.

The long-term stability of the graphene ink is an important parameter for reliable spraying and was investigated using OAS as precipitation of the ink would result in a lower concentration and absorbance, and with dynamic light scattering (DLS) to monitor the size and possible aggregation of the flakes. The Stokes-Einstein relation is used to estimate the average particle size in a dispersion, under the assumption of spherical particle shape, obtaining the intensity-weighted mean hydrodynamic size ( $Z$ ).<sup>71</sup> This makes, in principle, DLS unreliable to measure the average particle size of non-spherical flakes, such as in our case. However, it is possible to infer changes in the distribution of the dispersed flakes in our graphene ink caused by sedimentation or aggregation using DLS





**Fig. 1** (a) OAS of the LPE graphene ink diluted by a factor of 61. (b) DLS and OAS stability analysis. DLS indicates stability against aggregation, with  $<3\%$  decrease in relative size over 190 days whilst UV-Vis indicates gradual sedimentation initiating after 72 days of storage, peaking at  $-14.8\%$  at day 190. (c) AFM statistics showing a log-normal distribution of  $\langle S \rangle$  peaking at 190 nm. (d) AFM statistics showing a log-normal distribution of  $\langle t \rangle$  peaking at 2.65 nm, which equates to a mean of 5-layer thick graphene when adjusted for a 1 nm water layer. (e) TEM image of a typical LPE graphene flake before photonic annealing. (f) Raman spectra before and after photonic annealing.

by monitoring changes in the relative  $Z$  ( $Z_R$ ). For instance, an increase in the mean  $Z_R$  would indicate aggregate formation. Fig. 1b (top panel) plots the change in  $Z_R$  ( $\Delta Z_R$ ) with time, represented as the percentage change with respect to  $Z_R$  at the time of ink preparation. The graph shows that within a 190-day period,  $\Delta Z_R \sim -2.5 \pm 1\%$ , suggesting that only a minimal aggregate formation happens. Moreover, the graphene ink shows a monodisperse flake size profile indicated by a single peak in DLS measurement (Fig. S3a†). We also observed that the change in absorbance normalised to day 0 ( $\Delta A_R$ ) was  $\sim -14\%$  over a 190-day period (Fig. 1b, bottom panel), further demonstrating the stability of our graphene ink.

Fig. 1c and d show the atomic force microscopy (AFM) statistics (over 300 flakes) of the modal lateral flake size ( $\langle S \rangle$ ) and thickness ( $\langle t \rangle$ ), respectively, measured for our graphene ink deposited on a Si/SiO<sub>2</sub> substrate. Both the  $\langle S \rangle$  and  $\langle t \rangle$  have a log-normal distribution, which peak at  $\langle S \rangle \sim 190$  nm (Fig. 1c) and  $\langle t \rangle \sim 2.65$  nm (Fig. 1d), respectively. Assuming a water-layer flake thickness of 1 nm (ref. 72) and a graphene interlayer distance of 0.34 nm,<sup>73</sup> we obtain a mean flake thickness of 5 layers, indicating the graphene ink is composed of a combination of single-layer graphene (SLG) and few-layer graphene (FLG) flakes. This corresponds to an aspect ratio ( $A_r$ ) of  $\sim 67$  which is higher than that reported for graphene-NMP inks ( $\langle S \rangle = 121$  nm,  $\langle t \rangle = 6$  nm,  $A_r = 20$ ) under similar exfoliation conditions.<sup>74</sup> The  $\langle S \rangle$  is also measured using scanning electron microscopy (SEM) (Fig. S4†). A sample of 70 flakes was measured, obtaining a lognormal distribution peaking at  $\langle S \rangle$

$\sim 182$  nm which closely aligns with the values obtained from the AFM statistics. Transmission electron microscopy (TEM) was further used to image individual flakes, with a representative flake size of  $\langle S \rangle \sim 200$  nm shown in Fig. 1e.

The quality of the SLG and FLG flakes were monitored using Raman spectroscopy. Fig. 1f shows typical Raman spectra of the graphene ink deposited on SiO<sub>2</sub>, before and after photonic annealing (black and red curve respectively) to monitor any effect of the photonic annealing on the SLG/FLG flakes. The red and the black curves in Fig. 1f show the typical D peaks at  $\sim 1346$  cm<sup>-1</sup>, the 2D peaks at  $\sim 2690$  cm<sup>-1</sup>, and the G peaks at  $\sim 1581$  cm<sup>-1</sup> (red) and 1580 cm<sup>-1</sup> (black) respectively. The D peak shows a full-width at half maximum (FWHM) of 37.9 cm<sup>-1</sup> (red) and 38.9 cm<sup>-1</sup> (black). These values are consistent with those reported for LPE graphene inks,<sup>44,46,49</sup> indicating the high quality of the SLG and FLG flakes in the graphene inks and the absence of noticeable modification of the flakes upon photonic annealing.

## Device fabrication

Using a 6-step manufacturing process (Fig. 2), we developed a PCB test strip composed of two EG-GFET layouts (enabling up to two simultaneous EG-GFET measurements), each containing 4 electrodes – drain, source, gate, and quasi-reference (QR) (Fig. 3a). The test strip is manufactured using commercial PCB techniques on a glass-epoxy laminate substrate (FR-4). The EG-GFET source and drain interdigitated electrodes are comprised of 14 fingers, each 100  $\mu$ m wide, resulting in a channel



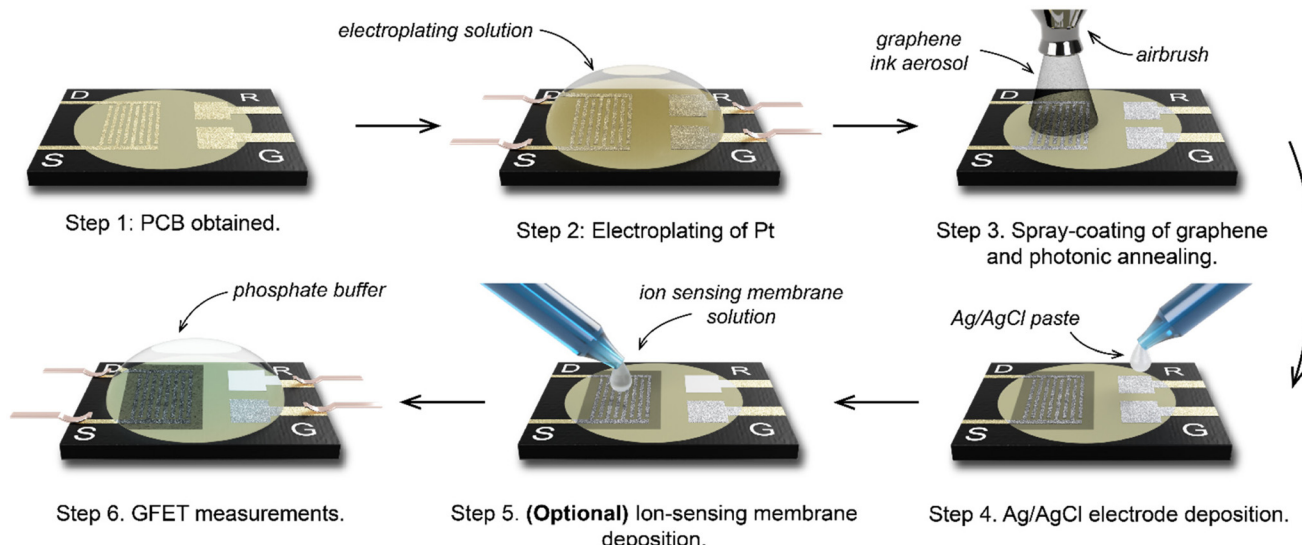


Fig. 2 The manufacturing process to make four-terminal graphene PCB transistors for chemical sensing.

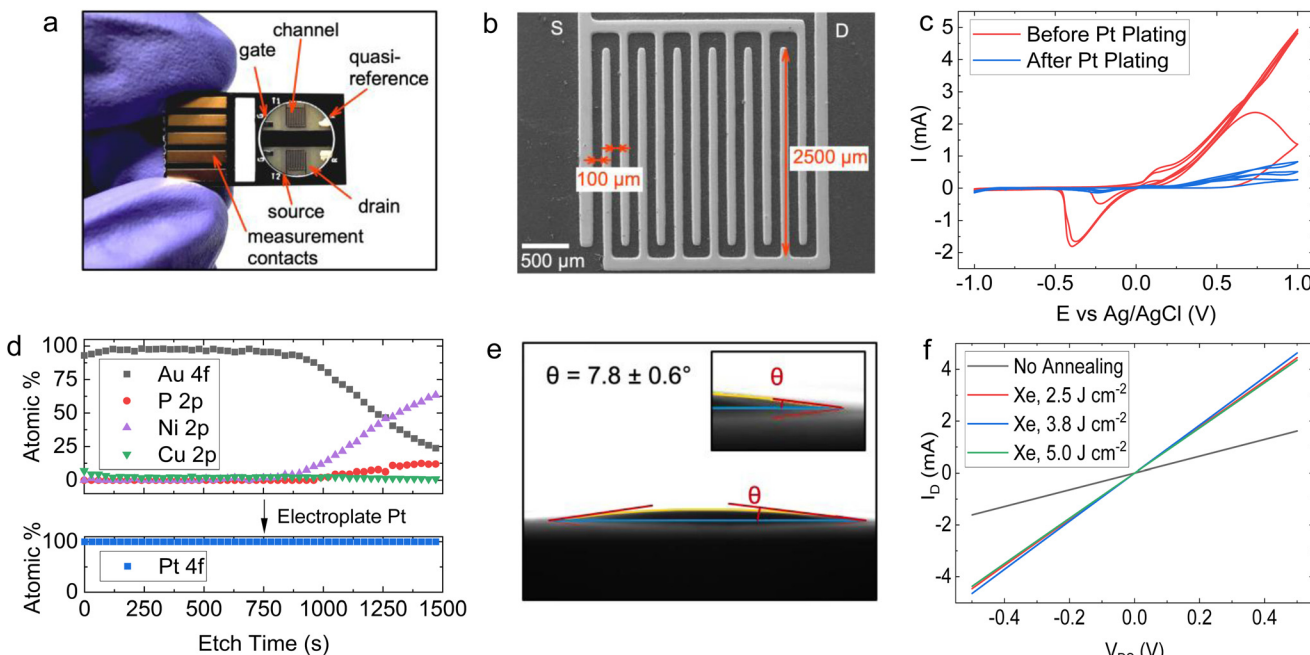


Fig. 3 (a) Photograph of the GFET on PCB. (b) SEM micrograph of the interdigitated electrodes. (c) Cyclic voltammetry between  $-1$  and  $1$  V using the original ENIG plated electrodes and Pt-plated electrodes, showing the nickel redox peaks and substantially greater stability of the Pt electrodes. (d) Depth profile of ENIG (top) and Pt (bottom) plating of the PCB. The approximate depth after 1500 seconds is  $120$  nm ( $0.08$  nm s $^{-1}$ ). (e) Contact angle of a drop of the graphene ink on a PCB substrate, showing a contact angle of  $\theta = 7.8 \pm 0.6^\circ$ . (f)  $I_D - V_{DS}$  curves for the graphene channel showing a change in resistance after IPL annealing. The electrodes were dry (not in a solution) during the measurement. The resistances were  $309.8$   $\Omega$  (not annealed) and  $112.4$ ,  $107.9$  and  $114.7$   $\Omega$  for light pulse energies of  $2.5$   $J$   $cm^{-2}$ ,  $3.75$   $J$   $cm^{-2}$  and  $5$   $J$   $cm^{-2}$ , respectively.

with  $100$   $\mu$ m length and  $2500$   $\mu$ m width (Fig. 3b). The overall channel area is  $3.25$   $mm^2$ . The gate and QR electrodes are  $1.25 \times 0.75$   $mm$ , and the QR electrode is covered with Ag/AgCl paste. The electrical connections to all electrodes are achieved using  $2.54$   $mm$ -spaced gold-plated contacts, designed to fit into standard card edge connectors.

Under ideal circumstances, the electrode surface must be inert under standard sensing conditions, to reduce the occurrence of undesirable chemical interference.<sup>75</sup> The surface of the PCB test strip electrodes is plated with a  $4$   $\mu$ m layer of nickel and a  $75$  nm layer of gold in a commercial electroless process (ENIG) to ensure the inertness of the electrodes,



similar to the process in ref. 76. However, clear Faradaic peaks from oxidation (at positive potentials *vs.* Ag/AgCl reference) and reduction ( $-0.4$  V *vs.* Ag/AgCl) of nickel or copper were observed (Fig. 3c, red curve) upon running cycling voltammetry in  $10\text{ mmol L}^{-1}$  phosphate buffer with the gate electrode as the working electrode and a carbon rod as the counter electrode. This experiment simulates the potentials the electrodes would be exposed to during EG-GFET measurements and, ideally, no peaks indicating the corrosion of the electrodes would be observed. The red curve in Fig. 3c shows that even at a low voltage of  $0.3$  V *vs.* Ag/AgCl, the electrodes would start to dissolve, interfering with the EG-GFET sensing. XPS depth profiling of the electrodes to approximately  $120$  nm depth revealed the presence of copper throughout (Fig. 3d, top) in addition to gold, likely coming from an uneven coverage of the gold layer. A layer containing nickel and phosphorus was observed approximately  $80$  nm below the surface which is expected. The ENIG gold plating process is primarily intended to improve the solderability of the PCBs rather than provide electrochemically inert electrodes, as reported previously.<sup>77</sup> Therefore, a  $0.5\text{ }\mu\text{m}$ -thick layer of platinum was electroplated onto all the electrodes, to render them inert (Fig. 2, step 2). XPS profiling the electroplated electrodes shows the presence of only pure platinum in the top  $120$  nm (Fig. 3d, bottom) and the cyclic voltammetry sweeps (Fig. 3c blue curve) show substantially reduced Faradaic currents, typically associated with water electrolysis on platinum electrodes.<sup>78</sup>

The EG-GFET channel is formed by automatic spray-coating (see 'Methods') to ensure repeatable and scalable deposition of graphene ink onto the PCB test strip (Fig. 2 step 3). The contact angle between the ink and the PCB surface was only  $7.8 \pm 0.6^\circ$  (Fig. 3e) and shows excellent wetting which contributes to film uniformity as the individual drops coalesce into a thin film before evaporating.<sup>45</sup> Furthermore, increasing the atomisation gas pressure, which is applied on the liquid being ejected from the nozzle, decreases the average droplet size of graphene ink, which contributes to the formation of films with uniform thickness by depositing a larger number of smaller droplets.<sup>45,60</sup> Therefore, the maximum pressure ( $275\text{ kPa}$ ) permitted by the setup was used. The distance between the air-brush and the substrate ( $40\text{ mm}$ ) was chosen such that the spray cone covered the entire area of the channel in a single pass. The spray rate was adjusted such that the film dried between the passes and the total volume of the ink was kept constant at  $0.4\text{ mL}$  to obtain approximately  $100\text{ }\Omega$  channel resistivity after photonic annealing. The repeatability of the spray coating is shown in Fig. S5 in ESI,<sup>†</sup> demonstrating an  $8\%$  standard deviation with respect to the mean electrical resistance of the sensor batch.

We investigated the effect of photonic annealing on the electrical resistance of the EG-GFET channel by exposing the PCB test strip to three different IPL energies (Fig. 3f). Xenon IPL exposure at  $2.5\text{ J cm}^{-2}$ ,  $3.75\text{ J cm}^{-2}$  and  $5.0\text{ J cm}^{-2}$  resulted in a similar decrease of the resistance from  $309.8\text{ }\Omega$  (not annealed, red curve) to  $112.4$ ,  $107.9$  and  $114.7\text{ }\Omega$  for light pulse energies of  $2.5\text{ J cm}^{-2}$ ,  $3.75\text{ J cm}^{-2}$  and  $5.0\text{ J cm}^{-2}$ , respectively.

Therefore, the lowest IPL energy ( $2.5\text{ J cm}^{-2}$ ) was used for all subsequent experiments, ensuring improved channel resistance with minimal risk of damage to the PCB.

## Device operation

The modular design of the PCB test strip increases the versatility of our platform – multi-sensor array test strips can be designed by multiplexing several EG-GFETs on the same PCB by proportionally increasing the quantity of source, drain electrodes. The EG-GFETs were contacted for electrical characterisation as shown in Fig. 4a. The QR electrode was connected to a high input impedance terminal ( $>1\text{ G}\Omega$  source meter unit input impedance) to ensure no current flows through it. Additionally, we measured the current flowing through the source, drain and gate electrodes to ensure a complete understanding of the device response (whether the observed current changes are actual modulation of the graphene channel or not), as recommended by ref. 79.

Our EG-GFETs were initially characterised in phosphate buffer (PB) solutions of  $10\text{ mmol L}^{-1}$  which is chosen as it provides a wide pH buffer range at around pH 7.<sup>80</sup> Fig. 4b shows the measured drain current ( $I_D$ ) plotted as a function of the gate voltage ( $V_{GS}$ ) at  $V_{DS} = +200\text{ mV}$ , over three forward (red curve) and backward (blue curve)  $V_{GS}$  sweep cycles between  $-500$  and  $+700\text{ mV}$ , demonstrating a typical ambipolar graphene field-effect behaviour at a fixed pH value of 7. The Dirac point (also referred to as the charge neutrality point or CNP) of the device at pH 7 is found at  $V_{GS} = +170\text{ mV}$  and  $130\text{ mV}$  for the forward sweep and backward sweep curves, respectively, showing a hysteresis of  $40\text{ mV}$ . The hysteresis observed is a well-known phenomenon in EG-GFETs. Computational modelling and Raman spectroscopy studies of the graphene-solution electrochemistry have suggested that the hysteresis is caused at least in part by electrochemical processes in the aqueous layer in contact with graphene.<sup>81,82</sup> The electrochemical reduction of oxygen,  $\text{O}_2 + 2\text{H}_2\text{O} + 4\text{e}^- = 4\text{OH}^-$ , occurs spontaneously at the graphene–water interface and it is thought to be the primary source of interference.<sup>81,83</sup> Reducing the dissolved oxygen content will result in a decrease in  $I_D$  and hysteresis but purging samples of dissolved oxygen would not be practical for real-world analysis at the point-of-care.<sup>84</sup> Consequently, we have arbitrarily chosen to conduct any further analysis on the EG-GFET sweep characteristics using the forward sweep, given the hysteresis effect does not appear to manifest in any drastic capacity at constant  $V_{GS}$ .

We then investigated the response of the EG-GFETs to changes in pH by changing the pH of the solution using a strong base or acid and monitoring the response. Fig. 4c plots the  $I_D$  as a function of  $V_{GS}$  of the EG-GFETs exposed to pH values ranging from 3 to 11 under a  $V_{DS} = +200\text{ mV}$ , which shows a shift of the Dirac point from  $60\text{ mV}$  to  $270\text{ mV}$ . Whilst pristine (defect-less) graphene should not respond to changes in pH,<sup>85</sup> the pH sensitivity is enabled by the type and density of unintentional defects imparted during the LPE process.<sup>86</sup> The corresponding pH-dependent shift in the Dirac point is shown in Fig. 4d, with a maximum Dirac point of  $270\text{ mV}$  at



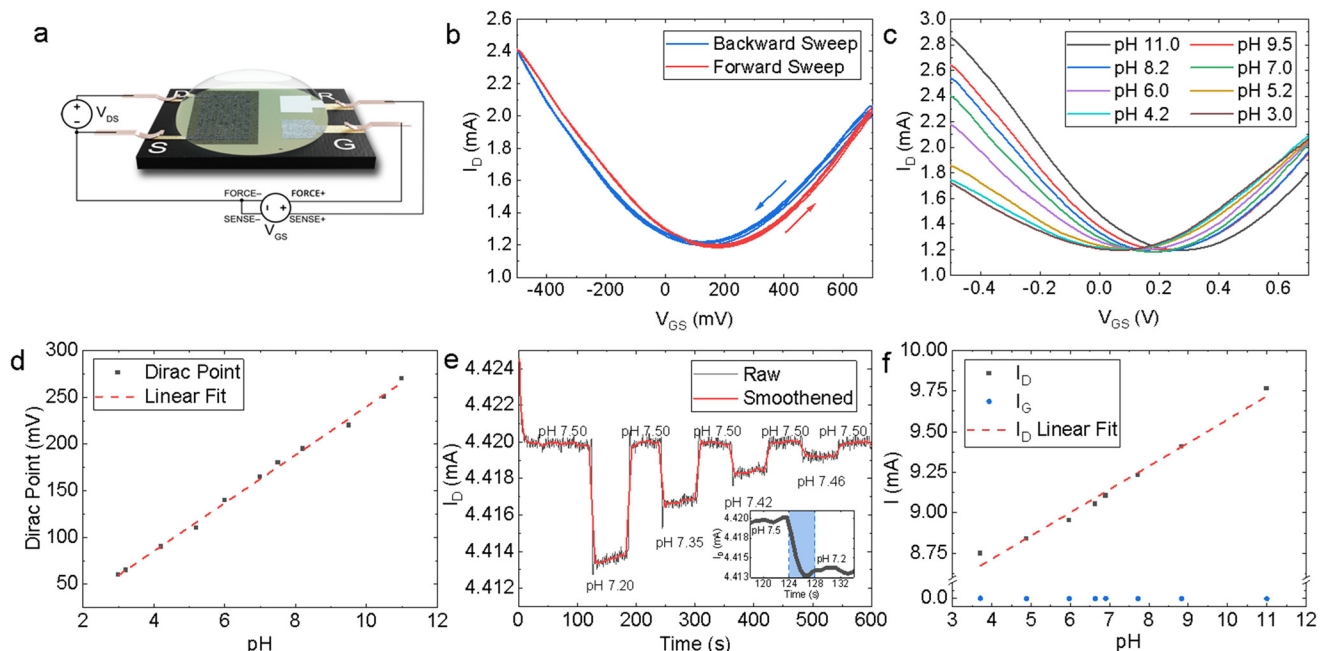


**Fig. 4** (a) Schematic of the four-terminal EG-GFET. (b) Forward and backward  $I_D$  vs.  $V_{GS}$  sweeps of the EG-GFET in 10 mmol  $L^{-1}$  PB solution at  $V_{DS} = +200$  mV. (c) Forward sweeps of the  $I_D$  vs.  $V_{GS}$  of the EG-GFET at decreasing pH values from pH 11 to pH 3. (d) The Dirac point values extracted from the plots in (c) showing a linearity of  $25.8 \pm 0.5$  mV per pH. (e) pH switching showing an ultimate resolution of 0.04 pH units, with response times of  $<10$  s. (f)  $I_D$  sensitivity of 143  $\mu$ A per pH through a linear range of pH 11 to pH 3 which is  $>2800$  times greater than the  $I_G$  response.

pH 11. A linear fit of the Dirac point values (red dashed line) reveals a sensitivity of  $25.8 \pm 0.5$  mV per pH, over a linear range of pH 11 to pH 3. This sensitivity is below the theoretical maximum predicted by the Nernst eqn (59.16 mV per pH)<sup>87</sup> and is higher than that observed for graphene pH sensors prepared by alternative graphene fabrication techniques such as CVD-grown graphene on  $\text{SiO}_2$  (21–22 mV per pH),<sup>88</sup> suspended graphene (17 mV per pH),<sup>89</sup> epitaxial graphene on silicon carbide (19 mV per pH)<sup>90</sup> and mechanically exfoliated graphene on  $\text{SiO}_2$  (20 mV per pH),<sup>91</sup> and within the same order of magnitude for reduced graphene oxide (rGO) based devices (29–40 mV per pH).<sup>92,93</sup>

We also use the  $V_{GS}$  sweeps to identify the ideal  $V_{GS}$  value for constant  $V_{GS}$  sensing. A  $V_{GS}$  value of +50 mV was chosen for pH sensing as it is in the linear regime of the  $I_D$  response and is also the  $V_{GS}$  at which the minimum magnitude of  $I_G$  occurs (Fig. S6†). The EG-GFET resolution to pH sensing is ultimately limited by the noise of the measurement setup.<sup>94</sup> Hence minimising  $I_G$  is integral to minimising noise and drift, improving device lifespan, and ensuring robustness.<sup>84,95</sup>

Fig. 4e shows the response of  $I_D$  (at  $V_{GS} = +50$  mV and  $V_{DS} = +200$  mV) as a function of time to diminishing alternate additions of acid and base, which change the pH of the measured solution. The baseline peak-to-peak  $I_D$  noise is  $I_{D,\text{noise},\text{P-P}} \sim 1$   $\mu$ A whilst root mean square (RMS)  $I_D$  noise is  $I_{D,\text{noise},\text{RMS}} \sim 0.2$   $\mu$ A. Adjusting the pH from 7.50 to 7.20 caused  $I_D$  to drop from 4.420 mA to 4.414 mA. The inset in Fig. 4e shows a zoomed-in region of the same plot for a pH change of 0.30 (blue shading) that we used to estimate the

response time as  $\tau_r \sim 4$  s. Subsequent adjustment of the pH from 7.20 back to 7.50 caused  $I_D$  to return to 4.420 mA. The resolution  $R$  was determined by measuring  $I_D$  over subsequent additions of acid and base in diminishing quantities, yielding  $R \sim 0.04$  pH units for the EG-GFET. Both  $\tau_r$  and  $R$  are in line with previously reported pH-sensitive EG-GFET devices,<sup>96</sup> demonstrating the suitability of our platform for commercial, scalable, and low-cost manufacturing techniques with superior performance characteristics to those based on CVD<sup>88</sup> and mechanical exfoliation.<sup>91</sup>

The sensitivity of the device may alternatively be described as a function of change in  $I_D$ , at constant  $V_{GS}$  and  $V_{DS}$ . Fig. 4f shows a plot of  $I_D$  values (black data points) as a function of pH at  $V_{DS} = +200$  mV and  $V_{GS} = +50$  mV. A linear fit (red dashed line) of the  $I_D$  points, shows a sensitivity of  $143 \pm 7$   $\mu$ A per pH through a dynamic range of pH 11.0 to 3.0. The sensitivity of  $I_D$  to pH is over three orders of magnitude higher than the sensitivity of  $I_G$  (blue data points), which is  $0.05 \pm 0.02$   $\mu$ A per pH over the same range, thus excluding the possibility of electrolysis playing a significant role in the sensor response to pH.<sup>79</sup> Moreover, we demonstrated multiple EG-GFETs detecting for pH ( $N = 10$ ) from 5 separate fabrication batches. The EG-GFETs were allowed to settle for 180 s to attain a stable  $I_D$  (Fig. S7†). The EG-GFETs show a mean pH sensitivity of sensitivity  $3.05 \pm 0.15\%$  per pH unit (Fig. S8†), between pH 3 and 11, with high precision and low variance (adjusted  $R^2 = 98.04\%$ ).

The utility of EG-GFETs resides in their versatility towards targeted detection of further species beyond  $\text{H}_3\text{O}^+/\text{OH}^-$  (pH).



We tested the suitability of our platform to detect  $\text{Na}^+$  by depositing a sodium-selective membrane as a proof-of-concept of the platform's potential use for ion-selective detection applications.<sup>97,98</sup> A thin polyvinyl chloride (PVC)-based ion selective membrane (ISM) impregnated with 'sodium ionophore X' (see 'Methods') was deposited on top of the graphene channel of the EG-GFET. In general, ion-selective EG-GFETs respond to the activity of the target ion with a higher sensitivity than other species, allowing for targeted measurements.<sup>97</sup> The extent of this selectivity depends on a range of factors including the membrane and analyte compositions.<sup>99</sup> In the ion-selective EG-GFET, a change of potential is experienced at the surface of the EG-GFET channel, which in turn is observed as a shift in the Dirac point and a subsequent change in  $I_D$ .<sup>100</sup>

The ion-selective EG-GFET was operated using the same electrical schematic shown in Fig. 4a. Fig. 5a shows three cycles of  $I_D$  plotted against the gate voltage ( $V_{GS}$ ) in a 10 mmol L<sup>-1</sup> potassium phosphate buffer (K-PB) solution, with the forward sweep (black curve) going from -500 mV to +700 mV and the backward sweep (red curve) going from +700 mV to -500 mV. The Dirac point is substantially broadened when compared to the membrane-less EG-GFET shown in Fig. 4b. Additionally, Fig. 5a shows an increased hysteresis between the forward and backward sweeps, resulting in the Dirac point shift for the forward sweep of more than +700 mV with respect to Ag/AgCl. However, the increased hysteresis did not influence the device performance, as  $\text{Na}^+$  quantification was conducted at constant  $V_{GS}$ .

Fig. 5b shows a decreasing  $I_D$  in response to incremental additions of  $\text{Na}^+$  to the ion selective EG-GFET at  $V_{DS} = +200$  mV and  $V_{GS} = +50$  mV. The LOD was measured as 5  $\mu\text{mol L}^{-1}$  for  $\text{Na}^+$ . The inset in Fig. 5b shows a zoomed-in region of the same plot for a change of 2 mmol L<sup>-1</sup>  $\text{Na}^+$  (green shading) that we used to estimate  $\tau_r \sim 15$  s, within the linear range of the ion selective EG-GFET. A plot of the  $I_D$  response as a function of  $\text{Na}^+$  concentration is plotted in Fig. 5c. The  $\text{Na}^+$  selective EG-GFET has a limit of quantification (LOQ) of 20  $\mu\text{mol L}^{-1}$ , with a log-linear response running from 20  $\mu\text{mol L}^{-1}$  to 10 mmol L<sup>-1</sup> (red dashed line) defining the device's linear range. The sensitivity of the device is extracted from the slope

of the response in Fig. 5b, which shows a sensitivity of  $131.4 \pm 5 \mu\text{A per } \log_{10}\text{Na}^+$ . These performance metrics are in line with the best sodium selective GFETs previously reported using CVD graphene.<sup>100,101</sup> Furthermore, we demonstrated 2  $\text{Na}^+$ -selective EG-GFETs simultaneously detecting  $\text{Na}^+$ . The EG-GFETs were allowed to settle for 300 s to attain a stable  $I_D$  (Fig. S9†). The EG-GFETs show a mean  $\text{Na}^+$  sensitivity of  $-6.58 \pm 0.19\%$  per  $\log_{10}$  change in  $\text{Na}^+$  concentration, between 5  $\mu\text{mol L}^{-1}$  and 10 mmol L<sup>-1</sup>, with high precision and low variance (adjusted  $R^2 = 99.43\%$ ).

The ion-selective EG-GFETs may be tuned by adjusting the chemical and physical composition of the ISMs, thus tailoring devices to meet specific application criteria for ion sensing. The versatility of ion selective detection is immediately evident for its utility in health but may also be of further use in environmental monitoring and veterinary care.<sup>102</sup> Moreover, our two pH and ion-selective EG-GFETs on the same PCB test strip demonstrate a platform structure that allows for the fabrication of multiple sensors which can detect multiple analytes within a sample, paving the way for high-performance, scalable commercial sensors for low-cost and real-time diagnostics.

### 3. Methods

#### Formulation of LPE Graphene Inks

50 mg mL<sup>-1</sup> of graphite (Ceylon) were added to 0.4 mg mL<sup>-1</sup> of polyvinyl-pyrrolidone (PVP) (Merck, average  $M_w = 40\,000$ ) in 2-propanol (Sigma Aldrich, ACS reagent  $\geq 99.8\%$  purity). The graphite was exfoliated by immersion of the mixture in a bath sonicator (Fisherbrand Elmasonic S150 Ultrasonication Unit, 300 W effective power) for 9 hours. The resultant dispersion was subsequently centrifuged (Beckman Allegra 64R, F06050 Fixed-Angle Rotor) at 13 000g (mean) for 1 hour. After centrifugation, the top 80% of the supernatant was retained as the LPE graphene ink.

#### Characterisation techniques

**Optical spectroscopy.** The flake concentration was estimated using an Agilent Cary 60 UV-Vis spectrophotometer in a quartz

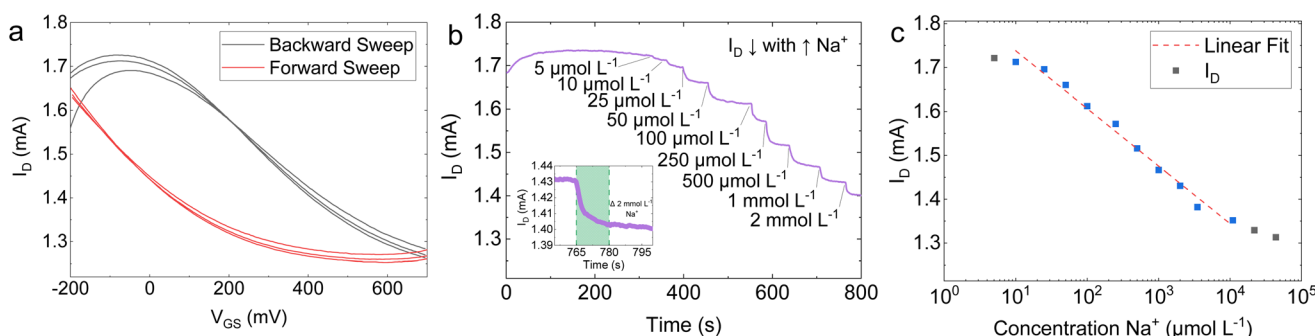


**Fig. 5** (a) Sweep of a  $\text{Na}^+$ -selective EG-GFET in 10 mmol L<sup>-1</sup> K-PB. (b) Incremental addition of  $\text{Na}^+$  results in a proportional decrease in the  $I_D$ . (c) The GFET response to  $\text{Na}^+$  is  $131.4 \pm 5 \mu\text{A per } \log_{10}\text{Na}^+$  in the range of 5  $\mu\text{mol L}^{-1}$  to 10 mmol L<sup>-1</sup>.



cuvette. Inks were appropriately diluted to ensure the region of interest had an absorbance value in the range of 0.1–1.0 where absorbance is approximately equal to the attenuation of the dispersion.<sup>103</sup> In the ink stability assays, OAS was used to supplement the DLS data, by analysing the rate of ink flake sedimentation in the ink as a function of the change in absorbance ( $\Delta A$ ). The relative absorbance ( $A_R$ ) is defined as the absorbance values normalised to the absorbance at day 1, with  $\Delta A_R$  subsequently defined as  $\Delta A_R = A_{R-1} - A_{R-x}$ , where  $A_{R-1}$  and  $A_{R-x}$  are the  $A_R$  at day 1 and the subsequent measurement day  $x$  respectively.

**Raman spectra** were measured on a Renishaw inVia micro-Raman spectrometer (WiRe 4.1) using a  $\times 20$  objective with a green 532 nm laser and 1800 lines per mm grating. An incident power of  $\leq 1$  mW was used to avoid thermal damage. Samples for Raman spectroscopy were deposited as thin films on Si/SiO<sub>2</sub> (Si-Mat, 200 nm dry thermal oxide).

**Dynamic light scattering** (DLS or photon correlation spectroscopy, PCS) was carried out on a Zetasizer Ultra. The scattering angle was set to 175°. Dispersions were freshly diluted in 0.4 mg mL<sup>-1</sup> PVP in IPA. Measurements were collected at 25 °C with 60 s of settling time. Stability assays were conducted by storing aliquots of inks in Eppendorf tubes under ambient conditions. Aliquots were retrieved over time and diluted for analysis. A dilution factor of 61 was determined by identifying the ink concentration range which yielded a constant  $Z$  average (Fig. S3b†). In the ink stability assays, the intensity-weighted mean hydrodynamic size ( $Z$ ) of the population of particles in a dispersion was used to infer changes in the distribution of SLGs and FLGs (brought about by sedimentation or aggregation) by monitoring the relative changes in  $Z$  with time, in conjunction with the sample's polydispersity. The relative  $Z$  ( $Z_R$ ) is defined as  $Z$  normalised to  $Z$  at day 1. Subsequently,  $\Delta Z_R$  is defined as  $\Delta Z_R = Z_{R-1} - Z_{R-x}$ , where  $Z_{R-1}$  and  $Z_{R-x}$  are the  $Z_R$  at day 1 and day  $x$  respectively.

**Electron microscopy.** Scanning electron microscopy (SEM) images were acquired using a LEO Gemini 1525 FEG-SEM. Images were collected by measuring secondary electrons using the In Lens and SE2 detectors respectively. Transmission electron microscopy images were acquired using a JEOL 2100Plus scanning transmission electron microscope. Dispersions of LPE graphene inks were diluted to 0.01 mg mL<sup>-1</sup> and deposited on holey carbon TEM grids (Agar Scientific, 200 mesh copper grids).

**Atomic force microscopy** (AFM) measurements were performed using the Asylum Research MFP 3D Scanning Probe Microscope. Measurements were collected in tapping mode using a general-purpose silicon AFM probe (Nanano SCOUT 70), with a 70 kHz resonance frequency and tip radius curvature of  $<10$  nm. LPE graphene dispersions were diluted to 0.01 mg mL<sup>-1</sup> and deposited on Si/SiO<sub>2</sub> (Si-Mat, 200 nm dry thermal oxide). Prior to deposition, the Si/SiO<sub>2</sub> wafers were cleaned of insoluble organic contaminants using a 5:1:1 mixture of deionised water, 30% (w/w) H<sub>2</sub>O<sub>2</sub> (Merck) and 25% ammonium hydroxide solution in water (Acros Organics, extra pure) at 80 °C for 10 minutes.<sup>104</sup> AFM analysis

was carried out using Gwyddion (v 2.58). The mean flake size  $\langle S \rangle$ , is calculated as  $\langle S \rangle = (\sum \sqrt{xy})/n$ , where  $x$  and  $y$  are the length and width of the flakes<sup>74</sup> and  $n$  is the number of flakes, while mean flake thickness  $\langle t \rangle$  is calculated by averaging the flake thickness at the thickest point for each flake. The aspect ratio ( $A_p$ ) was defined as  $\langle S \rangle/\langle t \rangle$ .

**Surface tension and contact angle measurements.** Surface tension measurements were measured using the pendant drop method using a FTA1000B imaging instrument (First Ten Angstroms) using the Drop Shape Analysis (v2.0) software. Drops were formed using a 20-gauge stainless steel dispenser needle. Using the same instrument and dispenser needle, drops were dropped onto a sample for contact angle measurements, the drop shape was imaged and the contact angle was determined using the FTA Drop Shape Analysis software.

**Rheological measurements.** A rheometer (HAAKE Mars 60) using a double coaxial cylinder geometry and the data fitted using a cross model to determine the infinite-rate viscosity. A double gap coaxial cylinder geometry is necessary for low viscosity inks which are not readily held within cone and plate, and parallel plate systems.<sup>105</sup> Moreover, such systems allow for better outflow controls at high shear rates whilst maintaining temperatures with improved uniformity.<sup>106</sup> All measurements were taken at 25 °C.

**X-ray photoelectron spectroscopy (XPS).** XPS spectra were acquired using the Thermo Scientific K-Alpha system incorporating a micro-focused Al K $\alpha$  X-ray source. The etching (profiling) was performed using the built-in argon ion sputtering gun, at 500 eV cluster energy and “medium” current setting, with an approximate 0.08 nm s<sup>-1</sup> etch rate. The analysis of graphene samples was performed on Si/SiO<sub>2</sub> substrates to avoid interfering signals from the FR-4 substrate and any silicon substrate signals were ignored for the purpose of quantitative analysis.

## Device fabrication

**PCB design.** A custom PCB design was created using Eagle CAD (Autodesk Inc., USA, v9.6.2). The source and drain were designed as an interdigitated electrode array with 100  $\mu$ m wide fingers and a channel with 100  $\mu$ m length and 2500  $\mu$ m width. Two further rectangular electrodes were added for separate gate and quasi-reference electrodes. The PCB designs were sent to a commercial foundry (Eurocircuits, Belgium) for manufacture using standard PCB processes. The substrate was FR-4 (a glass-epoxy laminate) and the 35  $\mu$ m copper was plated by the manufacturer with electroless nickel and gold coatings (ENIG) of 4  $\mu$ m and 75 nm, respectively.

**Electroplating.** The PCB electrodes were electroplated with platinum (Spa Plating Platinum Bath Solution) using a stainless-steel sheet counter electrode to improve their chemical inertness. Plating was done at a constant current of 1 mA for 30 minutes. The plating quality was inspected visually using optical microscopy and using XPS.

**Spray coating.** The graphene channel was deposited by spray coating the LPE graphene ink onto the interdigitated source-drain electrodes. The LPE graphene ink was spray-coated using



a custom-built automatic spray-coating setup consisting of an airbrush mounted on a movable platform with 3 axes of movement (XYZ) and with electronic gas flow control. The nozzle-substrate distance was chosen to 40 mm to cover the whole channel in a single pass. 275 kPa N<sub>2</sub> gas was used as the atomisation gas and using a 0.4 mm nozzle moving at 4000 mm min<sup>-1</sup> (the maximum movement speed the setup could achieve). The amount of ink pipetted into the spray-coater reservoir was kept constant at 0.4 mL to ensure repeatable deposition.

**Annealing.** Photonic annealing of the graphene film was performed using a xenon intense pulse light source (530–1400 nm) with <1.5 ms flash duration and a dose of 2.5–5 J cm<sup>-2</sup>. A steel stencil identical to the one used for spray-coating was used to selectively anneal the LPE graphene channel area.

**Reference electrode.** A 1  $\mu$ L drop of a commercial Ag/AgCl paste (Sun Chemical) was deposited on top of the PCB electrode denoted for the quasi-reference electrode, covering the entire electrode area with the Ag/AgCl paste. The device was then dried at 60 °C for 1 hour.

**Ion selective transistor.** The recipe for the sodium ion selective transistor was adapted from Choudhury *et al.*<sup>107</sup> In brief, a solution of 80 mg mL<sup>-1</sup> of the ion selective membrane was produced by dissolving 264 mg of polyvinyl chloride (PVC) (Sigma Aldrich, high molecular weight, Selectophore grade), 530 mg (1.24 mmol) of bis(2-ethylhexyl) sebacate (DOS) (Sigma Aldrich, selectophore grade) plasticiser, 5.6 mg (5.64  $\mu$ mol) of sodium ionophore X (IUPAC: 4-*tert*-butylcalix[4]arene-tetraacetic acid tetraethyl ester, Sigma Aldrich, selectophore grade), and 1.6 mg (3.23  $\mu$ mol) of potassium tetrakis ((4-chlorophenyl)-borate) (Sigma Aldrich, selectophore grade) ion exchanger in 10 mL of tetrahydrofuran (THF) (Sigma Aldrich, selectophore grade) and shaken for 10 minutes until the solution turned translucent. A 9 : 1 dilution in THF was conducted to produce a solution of 8 mg mL<sup>-1</sup>. The solution was stored at 2–8 °C.

The ion selective solution was deposited on top of the transistor by drop casting 5  $\mu$ L of the 8 mg mL<sup>-1</sup> solution onto the transistor and allowed 30 seconds to dry. A further 2.5  $\mu$ L of 80 mg mL<sup>-1</sup> was then deposited on top. The ion selective membrane (ISM) was allowed to dry for 12 hours in ambient conditions. Prior to first characterisation, the membranated devices were immersed for 15 minutes in a solution 0.1 mol L<sup>-1</sup> NaCl (VWR, ACS reagent) followed by a 10-minute rinse in deionised water. The sodium selective sensors were reused by dipping them in deionised water for 10 minutes.

## Device measurements

**Electrical measurements.** Electrical measurements of the graphene transistor devices were collected on a Keithley 4200 (Keithley Interactive Test Environment [KITE] v9.1), using a delay factor of 1.3, filter factor of 3 and A/D aperture times of 5 PLC. Measurements were taken at the lowest available source and current range. Measurements were taken at  $V_{DS}$  = +200 mV unless stated otherwise.

Peak to peak noise measurements were measured by measuring the difference between the maximum and

minimum values within a region where no response signal is expected. Alternatively, the RMS noise was measured as the standard deviation of the baseline noise since mean of a noise signal is zero.

**Sensor measurements.** Reference pH measurements were conducted in 0.01 mol L<sup>-1</sup> phosphate buffer (PB) solution using a Hanna Edge (HI2020) with a digital pH electrode with an integrated temperature sensor (HI11310). The pH electrode was calibrated daily using calibration solutions at pH 4.01, 7.01 and 10.01. The PB solution was prepared by dissolving 7.541 mmol of sodium phosphate dibasic heptahydrate, Na<sub>2</sub>HPO<sub>4</sub>·7H<sub>2</sub>O, (Sigma Aldrich, ACS reagent) and 2.459 mmol of sodium phosphate monobasic monohydrate, NaH<sub>2</sub>PO<sub>4</sub>·H<sub>2</sub>O, (Sigma Aldrich, ACS reagent, ≥98% purity) in 1 L of deionised water. pH adjustments were made by the appropriate addition of 1.0 mol L<sup>-1</sup> of orthophosphoric acid (Scientific Laboratory Supplies, 85% w/w) or 1.0 mol L<sup>-1</sup> sodium hydroxide solution (Scientific Laboratory Supplies, >99% purity).

Detection for sodium ions was conducted by sequential additions of Na<sub>2</sub>SO<sub>4</sub> (VWR, ≥98% purity) solutions in deionised water or potassium phosphate buffer solution (K-PB). K-PB was prepared by dissolving 7.541 mmol of potassium phosphate dibasic, K<sub>2</sub>HPO<sub>4</sub>, (Sigma Aldrich, ACS reagent, ≥98% purity) and 2.459 mmol of potassium phosphate monobasic, KH<sub>2</sub>PO<sub>4</sub>, (Sigma Aldrich, ACS reagent, ≥99%) in 1 L of deionised water.

For each detected analyte, the relevant device performance characteristics were established, in line with existing protocols.<sup>108,109</sup> The sensitivity is defined as the change in the device response divided by the corresponding change in stimulus, which is also expressed as the slope of the signal to stimulus.<sup>108,109</sup> The limit of detection (LOD) is the lowest amount of analyte that can be detected whilst the limit of quantification (LOQ) is the lowest amount of analyte that can be quantified.<sup>108</sup> The limit of quantitation (or quantification) is the analytical value above which greater values can be quantified.<sup>108</sup> The linear range is the range of analyte concentrations at which the signal response is linearly proportional to the concentration of analyte.<sup>108</sup> The resolution ( $R$ ) is defined as the lowest difference in concentration that can be distinguished on constant changes.<sup>109</sup> The response time ( $\tau_r$ ) is the time for a sensor to respond from a stable concentration of analyte to a step change in concentration.<sup>109</sup> Hysteresis is the maximum difference in output when a value is separately approached *via* increasing and decreasing analyte concentration ranges<sup>109</sup> or the maximum change in output between forward and backward  $V_{GS}$  sweeps at the same concentration.

## 4. Conclusions

This work demonstrates the first application of sprayed graphene transistors for test strips within a lab-on-PCB architecture for the detection of pH and selective ion sensing. We document a step-by-step procedure that makes use of commonly available chemicals, components, and techniques for



the fabrication of commercially viable, scalable, and low-cost chemical sensors and biosensors. By combining the production of graphene inks with spray coating, we can produce graphene transistor devices on PCB substrates. The test strips demonstrate sensing of pH between pH 3 and 11, with a resolution of 0.04 pH units, a response time of <10 seconds and a sensitivity of 25.8 mV per pH, which is in line with the state-of-the-art performances obtained using mechanically exfoliated and CVD-grown graphene. Finally, we also demonstrate the deposition of selective ion membranes on the surface of the graphene transistor for the detection of sodium as a proof-of-principle structure, with a sensitivity of  $131 \pm 4 \mu\text{A}$  per  $\log_{10}[\text{Na}^+]$  through a linear range of  $5 \mu\text{mol L}^{-1}$  to  $10 \text{ mmol L}^{-1}$ , setting the ground for commercially viable PCB-based sensor arrays.

## Author contributions

BFS and MH conceived and conducted the experiments, analysed the results, contributed to result interpretation and procedural validation. BFS also conducted the literature search. CY contributed to the characterisation of materials. FT directed the project, contributed to result interpretation and to procedural validation. BFS, MH, AEGC and FT wrote the manuscript with input from all the authors.

## Conflicts of interest

The authors have no conflicts of interest to declare.

## Acknowledgements

The authors would like to thank Prof. Milo Shaffer for access to the Raman spectroscopy suite, Dr Nicola Gasparini for his assistance with the electrical measurements. MH acknowledges funding from Imperial College President's PhD Scholarship (EPSRC EP/T51780X/1) and support by the EPSRC Centre for Doctoral Training in Advanced Characterisation of Materials (EPSRC EP/S023259/1). CY acknowledges funding from the China Scholarship Council. The authors acknowledge support from EPSRC grants EP/P02534X/2, EP/R511547/1 and EP/T005106/1, and the Imperial College Collaboration Kick-Start grant.

## References

- 1 A. van Belkum, T. T. Bachmann, G. Lüdke, J. G. Lisby, G. Kahlmeter, A. Mohess, K. Becker, J. P. Hays, N. Woodford, K. Mitsakakis, J. Moran-Gilad, J. Vila, H. Peter, J. H. Rex and W. M. Dunne, *Nat. Rev. Microbiol.*, 2019, **17**, 51–62.
- 2 A. A. Souza, C. Ducker, D. Argaw, J. D. King, A. W. Solomon, M. A. Biamonte, R. N. Coler, I. Cruz, V. Lejon, B. Levecke, F. K. Marchini, M. Marks, P. Millet, S. M. Njenga, R. Noordin, R. Paulussen, E. Sreekumar and P. J. Lammie, *Trans. R. Soc. Trop. Med. Hyg.*, 2021, **115**, 129–135.
- 3 P. A. Lieberzeit and F. L. Dickert, *Anal. Bioanal. Chem.*, 2009, **393**, 467–472.
- 4 S. Li, A. Simonian and B. A. Chin, *Electrochem. Soc. Interface*, 2010, **19**, 41–46.
- 5 N. Graber, H. Lodi and H. M. Widmer, *Sens. Actuators, B*, 1990, 239–243.
- 6 A. Vasilescu, P. Fanjul-Bolado, A. M. Titoiu, R. Porumb and P. Epure, *Chemosensors*, 2019, **7**(4), 66.
- 7 K. J. Land, D. I. Boeras, X. S. Chen, A. R. Ramsay and R. W. Peeling, *Nat. Microbiol.*, 2019, **4**, 46–54.
- 8 J. Janata, *Principles of Chemical Sensors*, 2009.
- 9 D. Grieshaber, R. MacKenzie, J. Vörös and E. Reimhult, *Sensors*, 2008, **8**, 1400–1458.
- 10 H. Lee, Y. J. Hong, S. Baik, T. Hyeon and D. H. Kim, *Adv. Healthc. Mater.*, 2018, **7**, 1701150.
- 11 Ö. Isildak and O. Özbek, *Crit. Rev. Anal. Chem.*, 2021, **51**, 218–231.
- 12 S. Das and V. Jayaraman, *Prog. Mater. Sci.*, 2014, **66**, 112–255.
- 13 T. Yang, R. Yu, Y. Yan, H. Zeng, S. Luo, N. Liu, A. Morrin, X. Luo and W. Li, *Sens. Actuators, B*, 2018, **274**, 501–516.
- 14 E. Sehit and Z. Altintas, *Biosens. Bioelectron.*, 2020, **159**, 112165.
- 15 J. Heikenfeld, A. Jajack, J. Rogers, P. Gutruf, L. Tian, T. Pan, R. Li, M. Khine, J. Kim, J. Wang and J. Kim, *Lab Chip*, 2018, **18**, 217–248.
- 16 A. J. Bandodkar, I. Jeerapan and J. Wang, *ACS Sens.*, 2016, **1**, 464–482.
- 17 H. Karimi-Maleh, F. Karimi, M. Alizadeh and A. L. Sanati, *Chem. Rec.*, 2020, **20**, 682–692.
- 18 B. Zhan, C. Li, J. Yang, G. Jenkins, W. Huang and X. Dong, *Small*, 2014, **10**, 4042–4065.
- 19 N. S. Green and M. L. Norton, *Anal. Chim. Acta*, 2015, **853**, 127–142.
- 20 M. Kaisti, *Biosens. Bioelectron.*, 2017, **98**, 437–448.
- 21 E. W. Hill, A. Vijayaraghavan and K. Novoselov, *IEEE Sens. J.*, 2011, **11**, 3161–3170.
- 22 V. Georgakilas, M. Otyepka, A. B. Bourlinos, V. Chandra, N. Kim, K. C. Kemp, P. Hobza, R. Zboril and K. S. Kim, *Chem. Rev.*, 2012, **112**, 6156–6214.
- 23 G. P. Nikoleli, Z. H. Ibupoto, D. P. Nikolelis, V. Likodimos, N. Psaroudakis, N. Tzamtzis, M. Willander and T. Hianik, *Cent. Eur. J. Chem.*, 2013, **11**, 1554–1561.
- 24 J. Ping, Y. Wang, K. Fan, W. Tang, J. Wu and Y. Ying, *J. Mater. Chem. B*, 2013, **1**, 4781–4791.
- 25 R. K. Paul, S. Badhulika, N. M. Saucedo and A. Mulchandani, *Anal. Chem.*, 2012, **84**, 8171–8178.
- 26 W. Fu, L. Jiang, E. P. van Geest, L. M. C. Lima, G. F. Schneider, W. Fu, L. Jiang, E. P. van Geest, L. M. C. Lima and G. F. Schneider, *Adv. Mater.*, 2017, **29**, 1603610.



27 B. Zhan, C. Li, J. Yang, G. Jenkins, W. Huang and X. Dong, *Small*, 2014, **10**, 4042–4065.

28 M. Khademi and D. P. J. Barz, *Langmuir*, 2020, **36**, 4250–4260.

29 M. Zhang, C. Liao, C. H. Mak, P. You, C. L. Mak and F. Yan, *Sci. Rep.*, 2015, **5**, 1–6.

30 H. U. Shihui, J. Zhang, Z. Wang and J. Yunfang, *Chin. J. Electron.*, 2022, **31**, 652–657.

31 F. Chen, Q. Qing, J. Xia, J. Li and N. Tao, *J. Am. Chem. Soc.*, 2009, **131**, 9908–9909.

32 A. Schuck, H. E. Kim, J. K. Moreira, P. S. Lora and Y. S. Kim, *Sensors*, 2021, **21**, 1–13.

33 C. Wang, X. Cui, Y. Li, H. Li, L. Huang, J. Bi, J. Luo, L. Q. Ma, W. Zhou, Y. Cao, B. Wang and F. Miao, *Sci. Rep.*, 2016, **6**, 21711.

34 C. F. Wang, X. Y. Sun, M. Su, Y. P. Wang and Y. K. Lv, *Analyst*, 2020, **145**, 1550–1562.

35 B. Cai, S. Wang, L. Huang, Y. Ning, Z. Zhang and G. J. Zhang, *ACS Nano*, 2014, **8**, 2632–2638.

36 R. Zhang and Y. Jia, *J. Instrum.*, 2021, **16**, P09021.

37 K. Maehashi, Y. Sofue, S. Okamoto, Y. Ohno, K. Inoue and K. Matsumoto, *Sens. Actuators, B*, 2013, **187**, 45–49.

38 X. Li, W. Cai, J. An, S. Kim, J. Nah, D. Yang, R. Piner, A. Velamakanni, I. Jung, E. Tutuc, S. K. Banerjee, L. Colombo and R. S. Ruoff, *Science*, 2009, **324**, 1312–1314.

39 Y. Zhang, L. Zhang and C. Zhou, *Acc. Chem. Res.*, 2013, **46**, 2329–2339.

40 Y. Hernandez, V. Nicolosi, M. Lotya, F. M. Blighe, Z. Sun, S. De, I. T. McGovern, B. Holland, M. Byrne, Y. K. Gun'ko, J. J. Boland, P. Niraj, G. Duesberg, S. Krishnamurthy, R. Goodhue, J. Hutchison, V. Scardaci, A. C. Ferrari and J. N. Coleman, *Nat. Nanotechnol.*, 2008, **3**, 563–568.

41 T. Hasan, F. Torrisi, Z. Sun, D. Popa, V. Nicolosi, G. Privitera, F. Bonaccorso and A. C. Ferrari, *Phys. Status Solidi B*, 2010, **2957**, 2953–2957.

42 F. Torrisi, T. Hasan, W. Wu, Z. Sun, A. Lombardo, T. S. Kulmala, G. W. Hsieh, S. Jung, F. Bonaccorso, P. J. Paul, D. Chu and A. C. Ferrari, *ACS Nano*, 2012, **6**, 2992–3006.

43 K. R. Paton, E. Varrla, C. Backes, R. J. Smith, U. Khan, A. O'Neill, C. Boland, M. Lotya, O. M. Istrate, P. King, T. Higgins, S. Barwick, P. May, P. Puczkarski, I. Ahmed, M. Moebius, H. Pettersson, E. Long, J. Coelho, S. E. O'Brien, E. K. McGuire, B. M. Sanchez, G. S. Duesberg, N. McEvoy, T. J. Pennycook, C. Downing, A. Crossley, V. Nicolosi and J. N. Coleman, *Nat. Mater.*, 2014, **13**, 624–630.

44 P. G. Karagiannidis, S. A. Hodge, L. Lombardi, F. Tomarchio, N. Decorde, S. Milana, I. Goykhman, Y. Su, S. v. Mesite, D. N. Johnstone, R. K. Leary, P. A. Midgley, N. M. Pugno, F. Torrisi and A. C. Ferrari, *ACS Nano*, 2017, **11**, 2742–2755.

45 T. Carey, C. Jones, F. le Moal, D. Deganello and F. Torrisi, *ACS Appl. Mater. Interfaces*, 2018, **10**, 19948–19956.

46 F. Torrisi, T. Hasan, W. Wu, Z. Sun, A. Lombardo, T. S. Kulmala, G.-W. Hsieh, S. Jung, F. Bonaccorso, P. J. Paul, D. Chu and A. C. Ferrari, *ACS Nano*, 2012, **6**, 2992–3006.

47 D. S. Kim, J. M. Jeong, H. J. Park, Y. K. Kim, K. G. Lee and B. G. Choi, *Nanomicro Lett.*, 2021, **13**, 1–14.

48 E. Jabari and E. Toyserkani, *Carbon*, 2015, **91**, 321–329.

49 T. Carey, S. Cacovich, G. Divitini, J. Ren, A. Mansouri, J. M. Kim, C. Wang, C. Ducati, R. Sordan and F. Torrisi, *Nat. Commun.*, 2017, **8**, 1–11.

50 E. B. Secor, P. L. Prabhmirashi, K. Puntambekar, M. L. Geier and M. C. Hersam, *J. Phys. Chem. Lett.*, 2013, **4**, 1347–1351.

51 S. Papamatthaiou, P. Estrela and D. Moschou, *Sci. Rep.*, 2021, **11**, 1–9.

52 V. Nicolosi, M. Chhowalla, M. G. Kanatzidis, M. S. Strano and J. N. Coleman, *Science*, 2013, **340**, 6139.

53 IEC 60747-14-10:2019, Semiconductor sensors. Performance evaluation methods for wearable glucose sensors.

54 N. Mavredakis, R. Garcia Cortadella, A. Bonaccini Calia, J. A. Garrido and D. Jiménez, *Nanoscale*, 2018, **10**, 14947–14956.

55 D. Moschou and A. Tserepi, *Lab Chip*, 2017, **17**, 1388–1405.

56 C. D. Chin, V. Linder and S. K. Sia, *Lab Chip*, 2012, **12**, 2118–2134.

57 H. J. Kim, K. A. Sudduth and J. W. Hummel, *J. Environ. Monit.*, 2009, **11**, 1810–1824.

58 C. Zuliani and D. Diamond, *Electrochim. Acta*, 2012, **84**, 29–34.

59 A. M. Zeidell, D. S. Filston, M. Waldrip, H. F. Iqbal, H. Chen, I. McCulloch and O. D. Jurchescu, *Adv. Mater. Technol.*, 2020, **5**, 2000390.

60 A. H. Lefebvre and V. G. McDonell, *Atomization and Sprays*, CRC Press, Boca Raton, 2nd edn, 2017.

61 I. M. Smallwood, *Handbook of Organic Solvent Properties*, 2012, pp. 1–306.

62 S. Bohm, A. Ingle, H. L. M. Bohm, B. Fenech-Salerno, S. Wu and F. Torrisi, *Philos. Trans. R. Soc., A*, 2021, **379**, 2203.

63 F. Torrisi and T. Carey, in *Flexible Carbon-Based Electronics*, ed. P. Samori and V. Palermo, Wiley-VCH, 2018, pp. 131–205.

64 M. Lotya, Y. Hernandez, P. J. King, R. J. Smith, V. Nicolosi, L. S. Karlsson, F. M. Blighe, S. De, W. Zhiming, I. T. McGovern, G. S. Duesberg and J. N. Coleman, *J. Am. Chem. Soc.*, 2009, **131**, 3611–3620.

65 A. B. Bourlinos, V. Georgakilas, R. Zboril, T. A. Steriotis, A. K. Stubos and C. Trapalis, *Solid State Commun.*, 2009, **149**, 2172–2176.

66 R. Narayan and S. O. Kim, *Nano Convergence*, 2015, **2**, 1–19.

67 B. K. Kandola, B. Biswas, D. Price and A. R. Horrocks, *Polym. Degrad. Stab.*, 2010, **95**, 144–152.

68 E. B. Secor, B. Y. Ahn, T. Z. Gao, J. A. Lewis and M. C. Hersam, *Adv. Mater.*, 2015, **27**, 6683–6688.



69 T. Stroucken and S. W. Koch, in *Optical Properties of Graphene*, ed. R. Bonder, World Scientific Publishing, 2016, pp. 43–84.

70 T. M. Aminabhavi, M. I. Aralaguppi, S. B. Harogoppad and R. H. Balundgi, *J. Chem. Eng. Data*, 1993, **38**, 31–39.

71 D. López-Díaz, M. López Holgado, J. L. García-Fierro and M. M. Velázquez, *J. Phys. Chem. C*, 2017, **121**, 20489–20497.

72 P. Nemes-Incze, Z. Osváth, K. Kamarás and L. P. Biró, *Carbon*, 2008, **46**, 1435–1442.

73 C. D. Reddy, S. Rajendran and K. M. Liew, *Nanotechnology*, 2006, **17**, 864–870.

74 T. Carey, S. Cacovich, G. Divitini, J. Ren, A. Mansouri, J. M. Kim, C. Wang, C. Ducati, R. Sordan and F. Torrisi, *Nat. Commun.*, 2017, **8**, 1201.

75 J. Barek, *Chemosensors*, 2021, **9**, 1–15.

76 A. Accogli, A. Lucotti and L. Magagnin, *ECS Trans.*, 2017, **75**, 1–6.

77 H. Shamkhalianchenar, C. J. Bueche and J. W. Choi, *Biosensors*, 2020, **10**, 159.

78 R. M. Cerviño, W. E. Triaca and A. J. Arvia, *J. Electroanal. Chem. Interfacial Electrochem.*, 1985, **182**, 51–60.

79 J. Janata, *ECS Solid State Lett.*, 2012, **1**, M29.

80 A. A. Green, *J. Am. Chem. Soc.*, 1933, **55**, 2331–2336.

81 H. Pinto, R. Jones, J. P. Goss and P. R. Briddon, *Phys. Status Solidi A*, 2010, **207**, 2131–2136.

82 H. Xu, Y. Chen, J. Zhang and H. Zhang, *Small*, 2012, **8**, 2833–2840.

83 J. Wei, B. Liang, Q. Cao, H. Ren, Y. Zheng and X. Ye, *Carbon*, 2020, **156**, 67–76.

84 A. Svetlova, D. Kireev, G. Beltramo, D. Mayer and A. Offenhäusser, *ACS Appl. Electron. Mater.*, 2021, **3**, 5355–5364.

85 W. Fu, C. Nef, O. Knopfmacher, A. Tarasov, M. Weiss, M. Calame and C. Schönenberger, *Nano Lett.*, 2011, **11**, 3597–3600.

86 W. Fu, C. Nef, A. Tarasov, M. Wipf, R. Stoop, O. Knopfmacher, M. Weiss, M. Calame and C. Schönenberger, *Nanoscale*, 2013, **5**, 12104–12110.

87 D. K. Harrison and W. F. Walker, *J. Med. Eng. Technol.*, 1980, **4**, 3–7.

88 B. Mailly-Giacchetti, A. Hsu, H. Wang, V. Vinciguerra, F. Pappalardo, L. Occhipinti, E. Guidetti, S. Coffa, J. Kong and T. Palacios, *J. Appl. Phys.*, 2013, **114**, 084505.

89 Z. Cheng, Q. Li, Z. Li, Q. Zhou and Y. Fang, *Nano Lett.*, 2010, **10**, 1864–1868.

90 J. Ristain, W. Zhang, F. Speck, M. Ostler, L. Ley and T. Seyller, *J. Phys. D: Appl. Phys.*, 2010, **43**, 345303.

91 Y. Ohno, K. Maehashi, Y. Yamashiro and K. Matsumoto, *Nano Lett.*, 2009, **9**, 3318–3322.

92 P. Salvo, N. Calisi, B. Melai, B. Cortigiani, M. Mannini, A. Caneschi, G. Lorenzetti, C. Paoletti, T. Lomonaco, A. Paolicchi, I. Scataglini, V. Dini, M. Romanelli, R. Fuoco and F. di Francesco, *Biosens. Bioelectron.*, 2017, **91**, 870–877.

93 I. Y. Sohn, D. J. Kim, J. H. Jung, O. J. Yoon, T. Nguyen Thanh, T. Tran Quang and N. E. Lee, *Biosens. Bioelectron.*, 2013, **45**, 70–76.

94 Y. Ohno, K. Maehashi and K. Matsumoto, *Biosens. Bioelectron.*, 2010, **26**, 1727–1730.

95 C. G. Jakobson, M. Feinsod and Y. Nemirovsky, *Sens. Actuators, B*, 2000, **68**, 134–139.

96 P. Salvo, B. Melai, N. Calisi, C. Paoletti, F. Bellagambi, A. Kirchhain, M. G. Trivella, R. Fuoco and F. di Francesco, *Sens. Actuators, B*, 2018, **256**, 976–991.

97 E. Bakker, P. Bühlmann and E. Pretsch, *Chem. Rev.*, 1997, **97**, 3083–3132.

98 P. Bühlmann, E. Pretsch and E. Bakker, *Chem. Rev.*, 1998, **98**, 1593–1687.

99 K. N. Mikhelson and M. A. Peshkova, *Russ. Chem. Rev.*, 2015, **84**, 555–578.

100 T. Huang, K. K. Yeung, J. Li, H. Sun, M. M. Alam and Z. Gao, *Nanomaterials*, 2022, **12**, 2620.

101 M. Xue, C. Mackin, W.-H. Weng, J. Zhu, Y. Luo, S.-X. L. Luo, A.-Y. Lu, M. Hempel, E. McVay, J. Kong and T. Palacios, *Nat. Commun.*, 2022, **13**, 5064.

102 G. Dimeski, T. Badrick and A. S. John, *Clin. Chim. Acta*, 2010, **411**, 309–317.

103 H. B. F. Dixon, *Pure Appl. Chem.*, 1992, **20**, 108.

104 X. Liang, B. A. Sperling, I. Calizo, G. Cheng, C. A. Hacker, Q. Zhang, Y. Obeng, K. Yan, H. Peng, Q. Li, X. Zhu, H. Yuan, A. R. Hight Walker, Z. Liu, L. M. Peng and C. A. Richter, *ACS Nano*, 2011, **5**, 9144–9153.

105 A. Ghanbari, Z. Mousavi, M. C. Heuzey, G. S. Patience and P. J. Carreau, *Can. J. Chem. Eng.*, 2020, **98**, 1456–1470.

106 P. Dontula, C. W. Macosko and L. E. Scriven, *J. Rheol.*, 2005, **49**, 807–818.

107 S. Choudhury, S. Roy, G. Bhattacharya, S. Fishlock, S. Deshmukh, S. Bhowmick, J. McLaughlin and S. S. Roy, *Electrochim. Acta*, 2021, **387**, 138341.

108 K. Danzer, *Analytical Chemistry, Theoretical and Metrological Fundamentals*, Springer, 2007.

109 M. Meister, A. Braun, B. Hüsing, U. Schmoch and T. Reiss, *Graphene and other 2D materials Technology and Innovation Roadmap Version 3*, 2017.

